Science and Technology of Advanced Materials

ISSN: (Print) (Online) Journal homepage: www.tandfonline.com/journals/tsta20

Chiral surface spin textures in Cu_2OSeO_3 unveiled by soft X-ray scattering in specular reflection geometry

V. Ukleev, C. Luo, R. Abrudan, A. Aqeel, C. H. Back & F. Radu

To cite this article: V. Ukleev, C. Luo, R. Abrudan, A. Aqeel, C. H. Back & F. Radu (2022) Chiral surface spin textures in Cu_2OSeO_3 unveiled by soft X-ray scattering in specular reflection geometry, Science and Technology of Advanced Materials, 23:1, 682-690, DOI: 10.1080/14686996.2022.2131466

To link to this article: https://doi.org/10.1080/14686996.2022.2131466

Published online: 20 Oct 2022.

SCIENCE AND TECHNOLOGY OF ADVANCED MATERIALS
2022, VOL. 23, NO. 1, 682–690
https://doi.org/10.1080/14686996.2022.2131466

Taylor & Francis
Taylor & Francis Group

Chiral surface spin textures in Cu_2OSeO_3 unveiled by soft X-ray scattering in specular reflection geometry

V. Ukleev[a], C. Luo[a,b], R. Abrudan[a], A. Aqeel[b,c], C. H. Back[b,c] and F. Radu[a]

[a]Helmholtz-Zentrum Berlin für Materialien und Energie, Berlin, Germany;
[b]Physik-Department, Technische Universität München, Garching, Germany;
[c]Munich Center for Quantum Science and Technology (MCQST), München, Germany

ABSTRACT

Resonant elastic soft X-ray magnetic scattering (XRMS) is a powerful tool to explore long-periodic spin textures in single crystals. However, due to the limited momentum transfer range imposed by long wavelengths of photons in the soft x-ray region, Bragg diffraction is restricted to crystals with the large lattice parameters. Alternatively, small-angle X-ray scattering has been involved in the soft energy X-ray range which, however, brings in difficulties with the sample preparation that involves focused ion beam milling to thin down the crystal to below a few hundred nm thickness. We show how to circumvent these restrictions using XRMS in specular reflection from a sub-nanometer smooth crystal surface. The method allows observing diffraction peaks from the helical and conical spin modulations at the surface of a Cu_2OSeO_3 single crystal and probing their corresponding chirality as contributions to the dichroic scattered intensity. The results suggest a promising way to carry out XRMS studies on a plethora of noncentrosymmetric systems hitherto unexplored with soft X-rays due to the absence of the commensurate Bragg peaks in the available momentum transfer range.

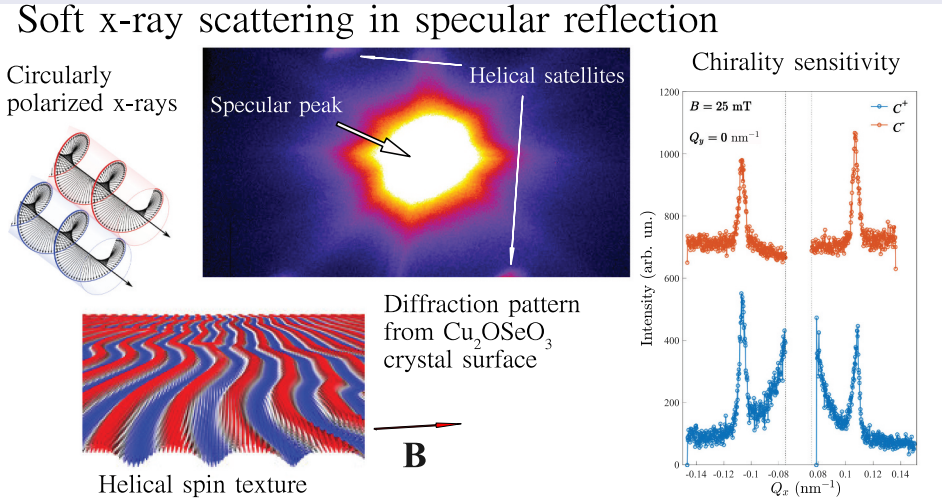

ARTICLE HISTORY
Received 3 July 2022
Revised 23 Sep 2022
Accepted 23 September 2022

KEYWORDS
X-ray resonant magnetic scattering; spin spirals; skyrmions; chirality; surface scattering; magnetic structure; soft X-ray diffraction

1. Introduction

Recently, noncentrosymmetric magnetic systems attracted attention due to the stabilization of topologically non-trivial spin textures through the antisymmetric Dzyaloshinskii-Moriya interaction (DMI) [1,2]. The competition between DMI symmetric exchange and temperature results in a variety of magnetic field induced topological spin-swirling textures, such as skyrmions, anti-skyrmions, bi-skyrmions, chiral bobbers, and merons [3].

The research on magnetic skyrmions has developed into two generic categories, namely, ordered skyrmion lattices in bulk non-centrosymmetric single crystals [4], and disordered skyrmion structures that occur in various ferromagnetic/heavy-metal multilayers and ferrimagnetic amorphous materials with controlled interfacial DMI that is induced by proximity to layers which exhibit a strong spin-orbit coupling [5–7]. The first category offers a versatile platform for studying fundamental collective traits of skyrmions through

CONTACT V. Ukleev v.ukleev@gmail.com; F. Radu florin.radu@helmholtz-berlin.de Helmholtz-Zentrum Berlin für Materialien und Energie, Berlin D-12489, Germany

specific methods such as neutron and x-ray scattering as well as ferromagnetic resonance [8], albeit often in a narrow temperature window that lies below room temperature. The second category emerged as an attractive route for applications in storage media since these skyrmions can be generated and controlled at room temperature in micro-structured devices [9].

B20-type cubic chiral magnets like MnSi [10], FeGe [11], FeCoSi [12] are prototype systems hosting Bloch-type skyrmions, while Néel-type ones were observed in polar lacunar spinels GaV_4S_8 [13], GaV_4Se_8 [14], and tetragonal $VOSe2O_5$ [15]. Cu_2OSeO_3 is one of the archetypal chiral skyrmion host, which differs drastically from the other B20 materials, despite belonging to the same chiral cubic space group $P2_13$ [16]. In contrast to the itinerant B20s, Cu_2OSeO_3 is a Mott insulator showing multiferroic properties and proven feasibility to control the skyrmion lattice phase by electric fields [16,17]. Moreover, in contrast to relatively isotropic B20-type magnets, Cu_2OSeO_3 shows a strongly anisotropic phase diagram at low temperatures exhibiting additional tilted conical [18], disordered skyrmions [19,20], and even square and elongated skyrmion phases [21,22], when the external magnetic field is applied along one of the cubic crystal axes. Furthermore, low Gilbert damping in Cu_2OSeO_3 allows investigations of skyrmion dynamics for high-frequency electronics and spintronics applications in the GHz frequency range [23,24]. These unique properties motivate a continuing exploration of Cu_2OSeO_3.

Over recent decades, X-ray resonant magnetic scattering (XRMS) method became a unique tool to investigate magnetic materials using polarized X-rays [25–30]. Although XRMS mechanisms are essentially the same across all spectral regions and experimental geometries, there are several aspects that distinguish their practical applications in studies of single crystals and in soft X-ray energy range. Firstly, long wavelengths of soft X-rays are limiting the accessible momentum transfer range Q, often leaving crystalline Bragg peaks outside of geometrical limits. It is worth to mention here that low-Q techniques such as small-angle scattering and reflectivity are well-suited for soft X-rays [31]. Secondly, a high absorption of soft X-rays limits XRMS studies to very thin (within 500 nm) specimens in transmission, or to surface layers in diffraction/reflection geometry. Nevertheless, XRMS has been proven effective for numerous element-specific studies of fundamental Fourier components of long-periodic magnetic structures in single-crystal chiral magnets by utilizing one of the available geometries [32–34]. Moreover, the possibility to tune the incident circular or linear polarization of the X-ray beam is particularly exciting for investigation of the topology of magnetic domain walls and winding numbers of the spin-swirling spin textures via circular dichroism [35–40].

As mentioned above, due to the high absorption at soft X-ray energies and limited momentum transfer range, two experimental XRMS geometries are typically utilized: 1) small-angle X-ray scattering from thinned crystals in transmission [33,41–46]; and 2) diffraction in the vicinity of a structural (or a magnetic) Bragg peak [36,38,47–50]. The latter is only applicable if Bragg reflection is allowed in the momentum transfer range available for the wavelength given at the resonant condition, e.g the L_3 or L_2 edges of a transition metal or the M_4 or M_5 edges of a rare-earth element. Up to date, the Bragg diffraction geometry was mainly utilized to study helical and skyrmion satellites of the anomalous reflection (001) in Cu_2OSeO_3. Moreover, information on the surface structure can be obtained by the diffuse surface X-ray scattering [51], and this method can be successfully extended to the study of the surface magnetic structure by studying the diffuse magnetic scattering at resonance [52,53]. For thin films and multilayers, the specular reflection [35,54,55] and multilayer Bragg sheet [39,40,56,57] geometries are utilized to detect magnetic satellites of the corresponding reflection.

So far, detection of the magnetic satellites in a specular reflection geometry from skyrmionic single crystal hosts has not been demonstrated in the soft X-ray region, mainly due to instruments availability and due to poor surface quality of the single crystals. Here, we show experimentally that for a crystal with sub-nm polished (001) Cu_2OSeO_3 surface, helical and conical magnetic modulations can be observed as satellite reflections around the specular peak (i.e. non-Bragg angle) and that chirality information of the underlying spin textures is encoded as dichroic intensity. This proof-of-principle experiment opens the possibility to explore a plethora of noncentrosymmetric systems hitherto unexplored with XRMS due to the absence of Bragg peaks in the available momentum transfer range at soft X-ray energies.

2. Materials and methods

A sketch of the experimental geometry is shown in Figure 1(a). The XRMS experiment was carried out at the dipole beamline PM-3 [58] of the BESSY II synchrotron (Helmholtz-Zentrum Berlin, Germany) using the recently commissioned ALICE-II station dedicated to soft X-ray scattering and coherent diffraction imaging, an upgraded version of ALICE [59]. The main new capability of ALICE-II is that the chamber accommodates a large scattered angle for the two-dimensional (2D) charge coupled device (CCD) detector (up to $2\theta = 144°$), as shown in Figure 1(b). This is achieved by choosing the entrance flange that meets the required reflected angle for the CCD. The CCD

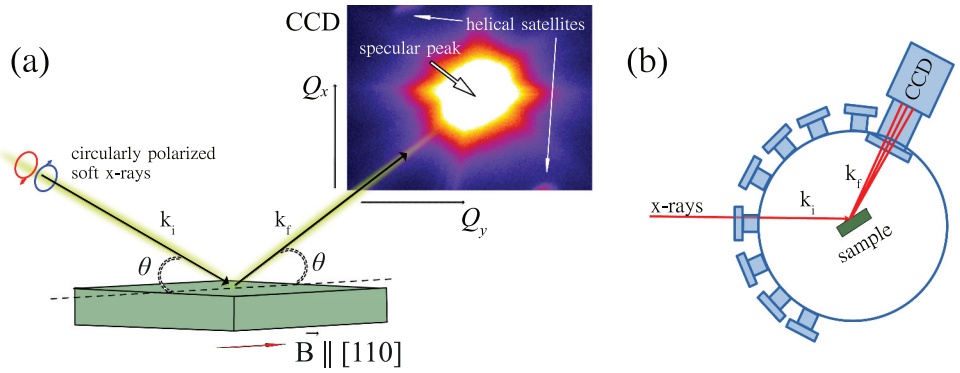

Figure 1. (a) Sketch of the experimental geometry. Circularly polarized soft X-rays impinge onto the samples at an angle θ and their specular reflection with off-specular magnetic satellites is detected by a position-sensitive 2D detector. The magnetic field **B** is applied along the in-plane [110] crystal axis. (b) Top view of the ALICE-II chamber (conceptual draw): the beam enters into the main chamber through a flange that can be selected to meet the required acceptance angle of the CCD detector.

itself can be mounted at two different distances with respect to the sample, namely at 28 cm and at 80 cm, referred to as *low-resolution* and *high-resolution* options, respectively. Recent upgrade of the endstation includes motorized beamstop available for both experimental configurations. Practically, in the *low-resolution* setting, the CCD chip can accommodate a reciprocal space representing up to ~8 nm lateral structures at a resonant energy of Cu, and for all available scattering angles.

For the current experiments, the chamber was mounted in the low resolution (high-Q range) configuration and the CCD detector of 2048 × 2048 pixels (Greateyes GmbH, Berlin, Germany) was centered at the scattering angle 2θ of 36°. An in-vacuum photodiode and total electron yield (TEY) detectors were used for the sample and chamber alignment with respect to the incident beam direction. The sample was consequently rotated around the θ axis to access the reciprocal space of interest, around the specular reflection. The base pressure in the chamber was 5×10^{-8} mbar.

The energy of the circularly polarized soft X-ray beam was tuned to the Cu L_3 edge at $E = 931.7$ eV to maximize the magnetic scattering intensity. The incoming beam was collimated by a pair of vertical slits in front of the chamber to reduce the incident beam divergence and hence to improve the angular resolution of the experiment. XRMS patterns were collected at the specular reflection condition (θ= 18°, 2θ= 36°) and symmetric off-specular $\pm Q_x$ regions (θ= 16°, 2θ= 36°) and (θ= 20°, 2θ= 36°) to cover the set of magnetic satellites.

The sample was mounted onto a dedicated sample holder and fixed by thermally and electrically conductive silver paint. The magnetic field was applied in the range of 0 − 270 mT along the [110] crystal axis using a rotatable electromagnet. The sample temperature was controlled by a close-cycle cryo-free cryostat (Stinger, ColdEdge Technologies, Allentown, USA). All measurements were carried out at the base temperature $T = 8$ K. The magnetic field dependencies of XRMS were measured for left and right circularly polarized soft x-rays. The acquisition time for each CCD image was 600 s. Detector images measured at $B = 200$ mT in the magnetic saturated sample state showing no incommensurate magnetic satellites were used to subtract the background. The aspect ratio of the images in the Q-space was corrected to account for the reflection geometry.

High-quality single enantiomer crystal Cu_2OSeO_3 was grown by chemical vapor transport (CVT) [60]. The crystal was oriented with a Laue diffractometer, cut into a cuboid shape with dimensions 5 × 3 × 1 mm^3, and mechanically polished [61]. The orientation of the polished surface was once again confirmed by X-ray Laue backscattering with sample edges oriented along ⟨110⟩ and ⟨001⟩ being along the out of plane crystallographic direction. The surface roughness of the sample was measured by atomic force microscopy (AFM) providing the root mean square value of 7 Å at the measured area of 50 × 50 μm^2 (Figure 2(a,b)). The surface quality was also confirmed with soft X-rays by means of rocking the sample about the specular reflection (Figure 2(c)). The rocking curve shows the full-width at half maximum (FWHM) of the specular reflection peak of 0.083° ± 0.002° confirming the excellent quality of the crystal surface. The width of a rocking curve defines the practical limitation of the method imposed by the overlap between the specular peak with magnetic satellites. The present quality of the crystal surface, and magnetic scattering intensity from helices in the Cu_2OSeO_3 crystal would allow one to resolve off-specular satellites formed by a spiral with a period λ up to $\lambda \approx 120$ nm. Although the mechanical polishing technique used in the present study does involve some damage of the crystal surface, most of the typical problems related to the surface quality could be avoided by the slow polishing speed.

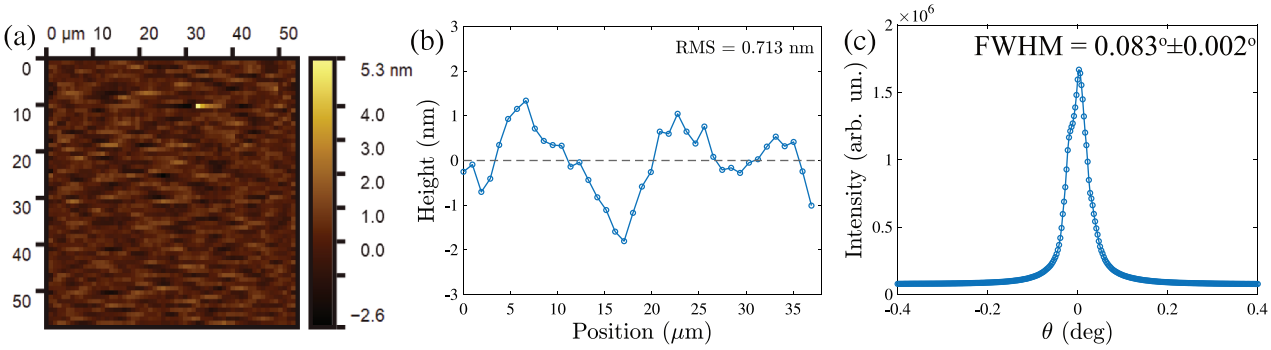

Figure 2. (a) AFM image of the polished Cu_2OSeO_3 crystal, demonstrating the exceptionally high quality of the sample's surface (0.7nm average roughness). (b) Representative line slice of the topography image. (c) Rocking curve measured around the specular peak.

Further improvement of the surface quality, such as removal of scratches by the ion beam or plasma jets [62] should be considered for higher resolution XRMS experiments in this geometry.

3. Results and discussions

3.1. Field dependence of magnetic satellite peaks in a reflection geometry

Typical magnetic phase diagram of Cu_2OSeO_3 at low temperatures for $\mathbf{B}||\langle 110\rangle$ consists of zero-field helical, field-induced conical and field-polarized phases [18]. Corresponding XRMS and small-angle neutron scattering patterns measured in the diffraction geometry can be found, for example in Refs. [63] and [18,19].

The XRMS patterns measured in the helical ground state at $B = 0$ mT and $T = 8$ K in the present study are shown in Figure 3(a) featuring four magnetic satellites arising from the proper screw spirals with a wavevector Q propagating along the in-plane crystallographic directions [100] and [010]. The spiral domain population is unbalanced between the two easy axes due to the magnetic field training applied to the sample during previous scans. Application of a moderate magnetic field of 20 mT along the middle axis [110] results in the re-orientation of the spiral domains. The re-population takes place due to an imperfect alignment of the magnetic field along the $\langle 110\rangle$, which favours the spiral domain with smaller angle between its propagation vector $\mathbf{Q}$ and direction of the magnetic field. Right before the transition to the conical phase at $B =$ 20 mT, we observe a fully saturated helical domain state (Figure 3(b)). Further increasing the magnetic field results in the transition to the conical state with $\mathbf{Q}||\mathbf{B}||[110]$ (Figure 3(c)). Hence, the helical to conical transition is divided into a two-step process. This process is reflected in the intensities of the peaks at $Q_y = \pm 0.04$ nm^{-1} showing an interplay in the magnetic field region between 0 and 20 mT (Figure 4(a)). Next, the more intense helical peak re-orients towards the field direction manifesting the first-

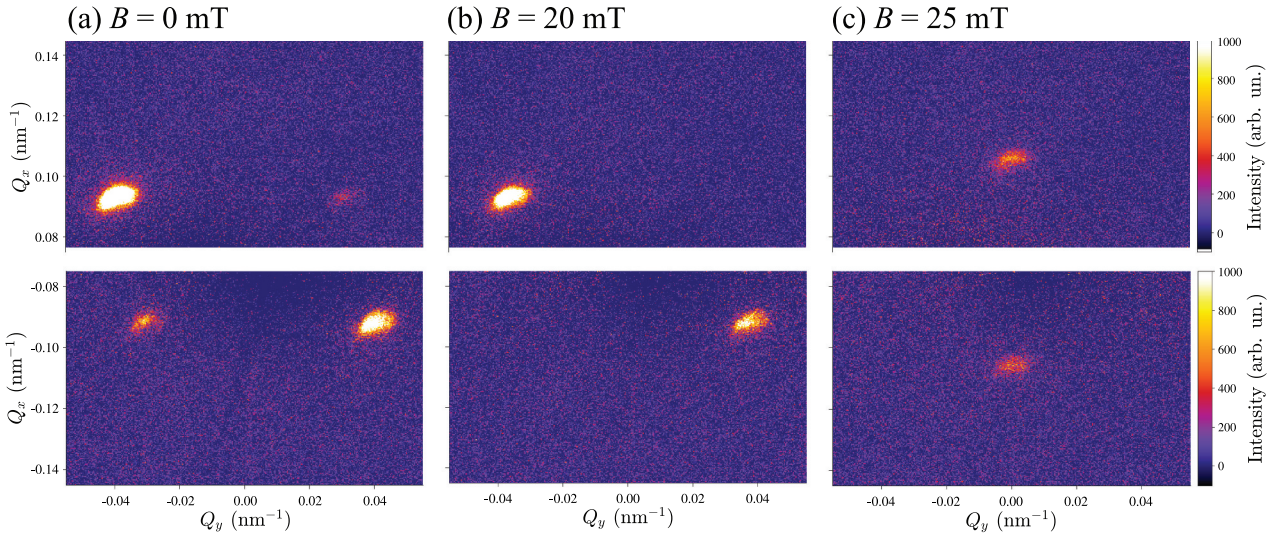

Figure 3. (Q_x, Q_y) maps of the XRMS intensity measured (a) in the multi-domain helical ($B = 0$ mT), (b) in the single-domain helicoidal ($B = 20$ mT), and (c) in the conical ($B = 25$ mT) states.

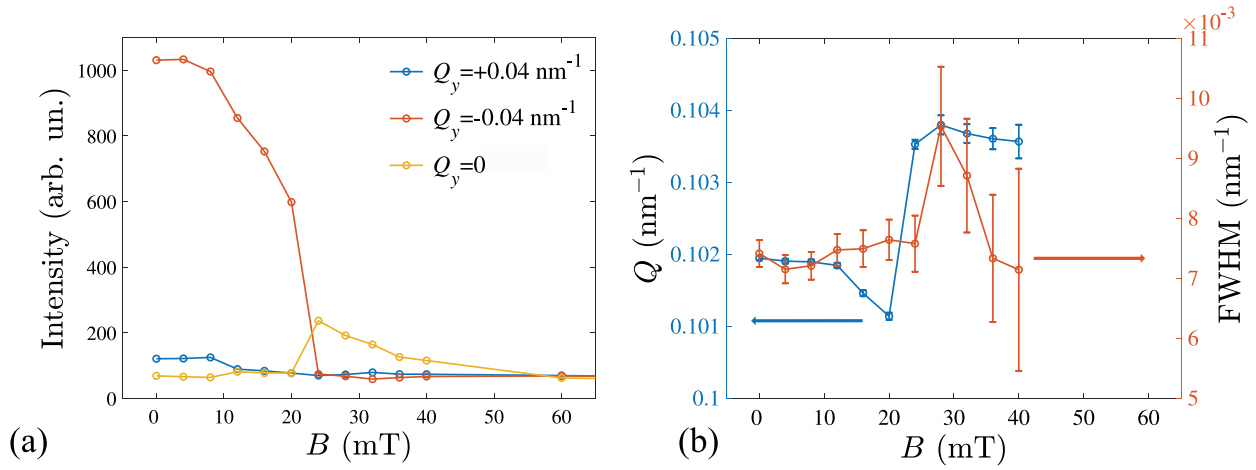

Figure 4. (a) Intensity, (b) position in the k-space (Q) and width (FWHM) of magnetic Bragg peaks vs. magnetic field dependencies in helical (0<B<20 mT) and conical (20<B<40 mT) states.

order helical to conical transition [64]. The magnitude of the spiral wavevector Q decreases as expected from the sine-Gordon law which is typical for chiral magnetic solitons (Figure 4(b)) [41,65,66]. Above the helical-to-conical transition field ($B>20$ mT) the intensity of the satellite peaks gradually decreases while their position remains unchanged as the magnetization approaches the field-induced ferromagnetic state (Figure 4). The slight increase of the conical Q-vector compared to the helical state (Figure 4(b)) is consistent with the previous observation in MnSi [67]. Interestingly, the widths of the helical and conical peaks are almost constant in the whole field range (Figure 4(b)). We note that in the present experiment the width of the satellite peaks is not limited by the instrument resolution or by the specular peak broadening, and reflects the coherent size of helical and conical domains. The apparent deviations from a gaussian peak structures in the Figure 4(b) are known to originate mainly from the intrinsic inhomogeneous shape of the incident beam.

3.2. Chirality sensitivity using circularly polarized light

Chirality of the magnetic structure is an important property of the helical and skyrmion phases. Magnetic chirality in cubic chiral Cu_2OSeO_3 is uniquely defined by the underlying chirality of the crystal structure [68]. X-ray magnetic scattering with polarized x-rays is an unique tool that can reveal the occurrence of chiral magnetic structure. In Figure 5(a) we show XRMS (symmetrical θ - 2θ scans along the Q_z direction) measured around the (001) Bragg peak of the crystal that was set in a helical phase at a temperature equal to 25 K in our previous experiment [8]. We probed three basic x-ray polarizations, namely circular positive (C^+), circular negative (C^-), and linear horizontal polarization (π). We observe that the intensity of the satellite magnetic peaks does exhibit a strong asymmetry: the intensity of the C^+ is lower with respect to the intensity of the C^- for the left side peak and this asymmetry change sign for the right side magnetic peak. The same scan performed with linearly polarized light shows, however, a symmetric intensity behavior. This asymmetry probed by circular light is a direct proof of chirality of the magnetic structure [35] and is fully consistent with the previous observation by Zhang et al [36]. The unique helicity of the magnetic structure, i.e. the absence of co-existing left and right chirality domains follows the single enantiomerism of the Cu_2OSeO_3 crystal. Further we show the chirality sensitivity away from the Bragg peak utilizing C^+ and C^- circularly polarized light.

Line profiles of the XRMS intensity of helical peaks at zero field along $\mathbf{Q}_y$ measured with two circular C^+ and C^- polarizations are shown in Figure 5(b). Intensity ratios between $+Q$ and $-Q$ peaks clearly change as the x-ray polarization is reversed. This is a result of two factors: re-population of helimagnetic domains by the field cycling between the measurements with C^+ and C^-, and actual circular dichroism of the XRMS intensity due to the topology of the chiral helical magnetic texture in Cu_2OSeO_3 [36]. From intensity profiles measured at the same field history (e.g. blue lines in Figure 5(b)) it is clear that the intensity ratios between the satellite magnetic peaks located at $Q_y = \pm 0.035$ nm^{-1} differ in the positive and negative intensity slices along $\mathbf{Q}_x$ and hence represent the actual chirality contribution to the XRMS effect, similar to the magnetic scattering around (001) Bragg peak (compare to Figure 5(a)).

The intensity difference between $+Q$ and $-Q$ satellite magnetic peaks belonging to the same helical or conical domain is expected due chirality of the magnetic texture. For the present experimental

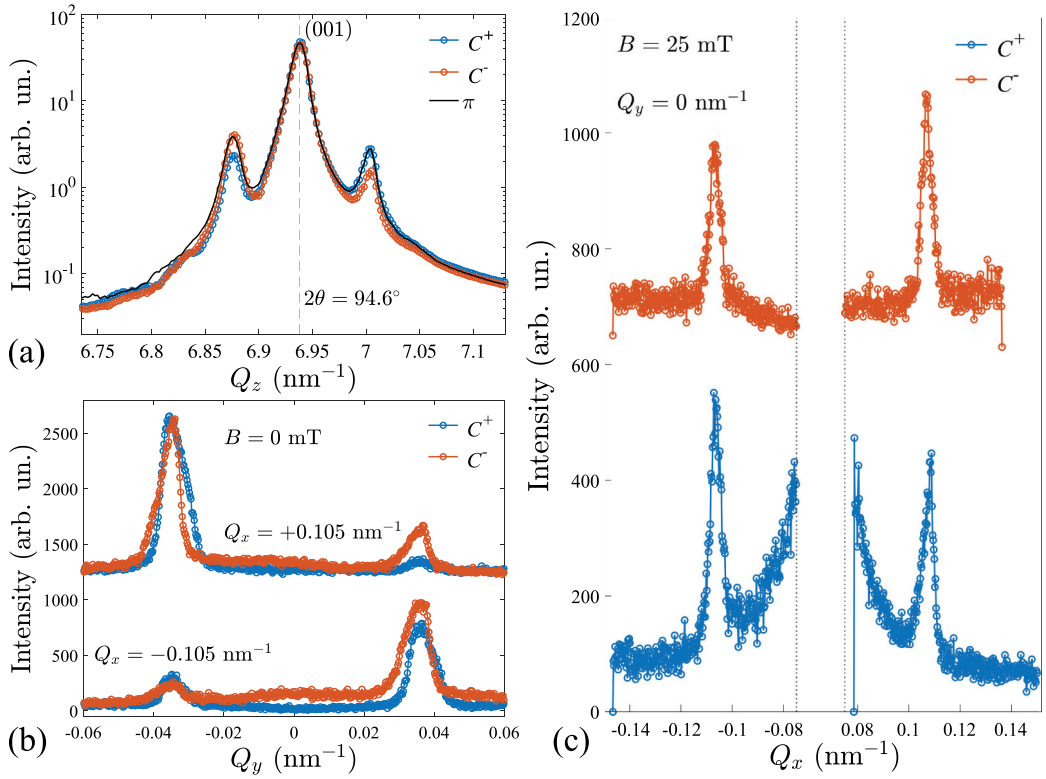

Figure 5. (a) Soft x-ray magnetic scattering (symmetrical scan along Q_z, i.e. θ - 2θ) in the helical phase, measured for a vanishing external magnetic field and at a temperature of 25 K. The intensity for the circular positive (C^+) and circular negative (C^-) x-ray helicity shows an asymmetric behavior on the magnetic satellites of (001) Bragg peak at $2\theta = 94.6°$. For linear (π) x-ray polarization, the intensities of the two side peaks are equal. This demonstrates the sensitivity to the chiral nature of the helical phase at the Bragg condition. (b) Line profiles of the specular-XRMS (non-Bragg) intensity along Q_y measured at $Q_x = \pm 0.105$ nm^{-1} with opposite C^+ and C^- polarizations at zero field. (c) Polarization-dependent line profiles of the XRMS intensity along Q_x measured at $Q_y = 0$ measured through the conical peaks at $B = 25$ mT.

geometry the dichroic contribution to the scattering intensity $I_{CD} = I_{C^-} - I_{C^+}$ reads as [36]

$$I_{CD} = -Y \sin^2 \xi \sin \theta \cos \psi, \quad (1)$$

where ξ is the conical angle and ψ is the azimuthal angle in the scattering plane ($\psi = 0$ corresponds to $\mathbf{Q}||\mathbf{Q}_x$), and Y is a constant determined by the XMCD contrast. In the case of a Bloch-type spin spiral which is characteristic to chiral magnets, the dichroic intensity follows a cosine law (Equation 1). This equation implies that the reflection geometry ($\theta \neq 0$) is necessary to detect a finite chiral contribution to XRMS, while in a transmission experiment the difference between I_{C^+} and I_{C^-} is dominated by other scattering mechanisms such as charge-magnetic interference [42,43,69]. Equation 1 also suggests that for the Bloch-type modulation, the maximum chirality contribution is expected at $\xi = 0$ and 180° which corresponds to the azimuthal angle of the satellite magnetic peaks in the conical state. Indeed, the intensity switching between C^+ and C^- in the conical state ($B = 25$ mT) is found in the line profiles of the XRMS intensity through $Q_y = 0$ (Figure 5(d)). The dichroic contribution to the intensity is also proportional to the conical angle and hence decreases as the system approaches the field-polarized state.

4. Conclusions

In conclusion, we have demonstrated a proof-of-principle resonant elastic soft x-ray scattering in specular reflection geometry on a polished single crystal of Cu_2OSeO_3. By measuring the satellite magnetic peaks at a base temperature of 8 K and as a function of an external field we have observed that the helical magnetic phase evolves from a multi-domain state to a single helical state, right before the eventual onset of the conical phase at $B = 20$ mT. This is a direct observation of a crossover from a multidomain to a fully saturated single helical domain phase across the large surface area probed by the x-ray beam. This new transition is proposed to originate from the imperfect alignment of the magnetic field along the ⟨110⟩ axis which favours energetically the spiral domain with the propagation vector that is oriented closer to the magnetic field direction. Moreover, we show that chirality information, for both helical and conical phases, is encoded in the asymmetric satellite peak intensities when comparing the scattering cross-

sections in a specular reflection geometry for circular positive with respect to circular negative x-ray beam polarizations. This is of key advantage since the intrinsic chirality of the system cannot be easily reversed through external stimuli.

The method provides a way to investigate long-periodic charge, orbital, and spin modulations in the near-surface regions of polished single crystals, thin films, and multilayers. XRMS in a specular reflection geometry is interesting in relation to spin textures in hitherto unexplored non-centrosymmetric magnets with resonant soft x-ray scattering, including depth-sensitive dichroic techniques [48]. Particularly, materials whose lattice parameters do not allow soft x-ray experiments in the Bragg diffraction geometry, such as chiral MnSi [10], FeGe [11], FeCoSi [12], CoZnMn [70], polar GaV_4S_8 [13], $VOSe_2O_5$ [15], and D_{2d} $Mn_{1.4}PtSn$ [71], $Cr_{11}Ge_{19}$ [71,72], $Fe_{1.9}Ni_{0.9}Pd_{0.2}P$ [73] are all promising candidates for future structural and dynamics studies using the method reported here. Furthermore, the ALICE-II diffractometer equipped with the 2D detector provides a great opportunity for the real-space imaging in reflection geometry by exploiting coherence of modern synchrotron undulator beamlines.

Acknowledgement

We would like to thank Torsten Kachel (BESSY II) for his help with the beamline operation.

Disclosure statement

No potential conflict of interest was reported by the author(s).

Funding

We acknowledge financial support for the VEKMAG project and for the PM2-VEKMAG beamline by the German Federal Ministry for Education and Research (BMBF 05K2010, 05K2013, 05K2016, 05K2019) and by HZB. F.R. acknowledge funding by the German Research Foundation via Project No. SPP2137/RA 3570. This work has also been funded by the Deutsche Forschungsgemeinschaft (DFG, German Research Foundation) under SPP2137 Skyrmionics and the excellence cluster MCQST under Germany's Excellence Strategy EXC-2111 (Project No. 390814868).

ORCID

V. Ukleev http://orcid.org/0000-0003-3703-264X

References

[1] Bogdanov A, Hubert A. Thermodynamically stable magnetic vortex states in magnetic crystals. J Magn Magn Mater. 1994;138(3):255–269.
[2] Nagaosa N, Tokura Y. Topological properties and dynamics of magnetic skyrmions. Nat Nanotechnol. 2013;8(12):899.
[3] Göbel B, Mertig I, Tretiakov OA. Beyond skyrmions: review and perspectives of alternative magnetic quasiparticles. Phys Rep. 2021;895:1–28.
[4] Tokura Y, Kanazawa N. Magnetic skyrmion materials. Chem Rev. 2020;121:2857–2897.
[5] Fert A, Reyren N, Cros V. Magnetic skyrmions: advances in physics and potential applications. Nature Rev Mater. 2017;2(7):1–15.
[6] Büttner F, Lemesh I, Beach GS. Theory of isolated magnetic skyrmions: from fundamentals to room temperature applications. Sci Rep. 2018;8:1–12.
[7] Wu H, Groß F, Dai B, et al. Ferrimagnetic skyrmions in topological insulator/ferrimagnet heterostructures. Adv Mater. 2020;32(34):2003380. DOI:10.1002/adma.202003380
[8] Pöllath S, Aqeel A, Bauer A, et al. Ferromagnetic resonance with magnetic phase selectivity by means of resonant elastic x-ray scattering on a chiral magnet. Phys Rev Lett. 2019;123(16):167201.
[9] Luo S, You L. Skyrmion devices for memory and logic applications. APL Mater. 2021;9(5):050901.
[10] Muhlbauer S, Binz B, Jonietz F, et al. Skyrmion lattice in a chiral magnet. Science. 2009;323(5916):915–919.
[11] Yu XZ, Kanazawa N, Onose Y, et al. Near room-temperature formation of a skyrmion crystal in thin-films of the helimagnet FeGe. Nat Mater. 2011;10(2):106–109.
[12] Münzer W, Neubauer A, Adams T, et al. Skyrmion lattice in the doped semiconductor $Fe_{1-x}Co_xSi$. Phys Rev B. 2010;81:041203.
[13] Kézsmárki I, Bordács S, Milde P, et al. Néel-type skyrmion lattice with confined orientation in the polar magnetic semiconductor GaV_4S_8. Nat Mater. 2015;14(11):1116–1122. DOI:10.1038/nmat4402
[14] Fujima Y, Abe N, Tokunaga Y, et al. Thermodynamically stable skyrmion lattice at low temperatures in a bulk crystal of lacunar spinel GaV_4Se_8. Phys Rev B. 2017;95(18):180410.
[15] Kurumaji T, Nakajima T, Ukleev V, et al. Néel-type skyrmion lattice in the tetragonal polar magnet $VOSe_2O_5$. Phys Rev Lett. 2017;119(23):237201.
[16] Seki S, Yu XZ, Ishiwata S, et al. Observation of skyrmions in a multiferroic material. Science. 2012;336(6078):198–201.
[17] White JS, Levatić I, Omrani A, et al. Electric field control of the skyrmion lattice in Cu_2OSeO_3. J Phys. 2012;24(43):432201. DOI:10.1088/0953-8984/24/43/432201
[18] Qian F, Bannenberg LJ, Wilhelm H, et al. New magnetic phase of the chiral skyrmion material Cu_2OSeO_3. Sci Adv. 2018;4(9):eaat7323. DOI:10.1126/sciadv.aat7323
[19] Chacon A, Heinen L, Halder M, et al. Observation of two independent skyrmion phases in a chiral magnetic material. Nat Phys. 2018;14:936–941.
[20] Bannenberg LJ, Wilhelm H, Cubitt R, et al. Multiple low-temperature skyrmionic states in a bulk chiral magnet. Npj Quantum Mater. 2019;4:1–8.
[21] Takagi R, Yamasaki Y, Yokouchi T, et al. Particle-size dependent structural transformation of skyrmion lattice. Nat Commun. 2020;11(1):1–7.
[22] Aqeel A, Sahliger J, Taniguchi T, et al. Microwave spectroscopy of the low-temperature skyrmion state in Cu_2OSeO_3. Phys Rev Lett. 2021;126:017202.

[23] Schwarze T, Waizner J, Garst M, et al. Universal helimagnon and skyrmion excitations in metallic, semiconducting and insulating chiral magnets. Nat Mater. 2015;14:478–483.
[24] Mochizuki M, Seki S. Dynamical magnetoelectric phenomena of multiferroic skyrmions. J Phys. 2015;27:503001.
[25] Stirling W, Cooper M. X-ray magnetic scattering. J Magn Magn Mater. 1999;200:755–773.
[26] Kortright J, Awschalom D, Stöhr J, et al. Research frontiers in magnetic materials at soft x-ray synchrotron radiation facilities. J Magn Magn Mater. 1999;207:7–44.
[27] Ament LJ, Van Veenendaal M, Devereaux TP, et al. Resonant inelastic x-ray scattering studies of elementary excitations. Rev Mod Phys. 2011;83:705.
[28] Vettier C. Resonant elastic x-ray scattering: where from? where to? Eur Phys J Spec Top. 2012;208:3–14.
[29] Fink J, Schierle E, Weschke E, et al. Resonant elastic soft x-ray scattering. Rep Prog Phys. 2013;76:056502.
[30] Ohsumi H, Arima TH. Novel insight into structural magnetism by polarized synchrotron x-ray scattering. Adv Phys X. 2016;1:128–145.
[31] Kortright JB. Resonant soft x-ray and extreme ultraviolet magnetic scattering in nanostructured magnetic materials: fundamentals and directions. J Electron Spectros Relat Phenomena. 2013;189:178–186.
[32] Mulders AM, Lawrence SM, Princep AJ, et al. Circularly polarized soft x-ray diffraction study of helical magnetism in hexaferrite. Phys Rev B. 2010;81:092405.
[33] Yamasaki Y, Morikawa D, Honda T, et al. Dynamical process of skyrmion-helical magnetic transformation of the chiral-lattice magnet fege probed by small-angle resonant soft x-ray scattering. Phys Rev B. 2015;92:220421.
[34] Ueda H, Skoropata E, Burian M, et al. Conical spin order with chiral quadrupole helix in $CsCuCl_3$. Phys Rev B. 2022;105:144408.
[35] Durr H, Dudzik E, Dhesi S, et al. Chiral magnetic domain structures in ultrathin FePd films. Science. 1999;284:2166–2168.
[36] Zhang S, Bauer A, Berger H, et al. Resonant elastic x-ray scattering from the skyrmion lattice in Cu_2OSeO_3. Phys Rev B. 2016;93:214420.
[37] Zhang S, van der Laan G, Hesjedal T. Direct experimental determination of spiral spin structures via the dichroism extinction effect in resonant elastic soft x-ray scattering. Phys Rev B. 2017;96:094401.
[38] Zhang S, Van Der Laan G, Hesjedal T. Direct experimental determination of the topological winding number of skyrmions in Cu_2OSeO_3. Nat Commun. 2017;8:1–7.
[39] Chauleau JY, Legrand W, Reyren N, et al. Chirality in magnetic multilayers probed by the symmetry and the amplitude of dichroism in x-ray resonant magnetic scattering. Phys Rev Lett. 2018;120:037202.
[40] Legrand W, Chauleau JY, Maccariello D, et al. Hybrid chiral domain walls and skyrmions in magnetic multilayers. Sci Adv. 2018;4:eaat0415.
[41] Okamura Y, Yamasaki Y, Morikawa D, et al. Emergence and magnetic-field variation of chiral-soliton lattice and skyrmion lattice in the strained helimagnet Cu_2OSeO_3. Phys Rev B. 2017;96:174417.
[42] Ukleev V, Yamasaki Y, Morikawa D, et al. Coherent resonant soft x-ray scattering study of magnetic textures in FeGe. Quantum Beam Sci. 2018;2:3.
[43] Ukleev V, Yamasaki Y, Morikawa D, et al. Element-specific soft x-ray spectroscopy, scattering, and imaging studies of the skyrmion-hosting compound $Co_8Zn_8Mn_4$. Phys Rev B. 2019;99:144408.
[44] Burn D, Zhang S, Wang S, et al. Helical magnetic ordering in thin fege membranes. Phys Rev B. 2019;100:184403.
[45] Burn DM, Wang S, Wang W, et al. Field and temperature dependence of the skyrmion lattice phase in chiral magnet membranes. Phys Rev B. 2020;101:014446.
[46] Ukleev V, Yamasaki Y, Utesov O, et al. Metastable solitonic states in the strained itinerant helimagnet FeGe. Phys Rev B. 2020;102:014416.
[47] Langner M, Roy S, Mishra S, et al. Coupled skyrmion sublattices in Cu_2OSeO_3. Phys Rev Lett. 2014;112:167202.
[48] Zhang S, van der Laan G, Müller J, et al. Reciprocal space tomography of 3D skyrmion lattice order in a chiral magnet. Proc Nat Acad Sci. 2018;115:6386–6391.
[49] Zhang S, Burn DM, Jaouen N, et al. Robust perpendicular skyrmions and their surface confinement. Nano Lett. 2020;20:1428–1432.
[50] Burn D, Brearton R, Ran K, et al. Periodically modulated skyrmion strings in Cu_2OSeO_3. Npj Quantum Mater. 2021;6:1–8.
[51] Renaud G, Lazzari R, Leroy F. Probing surface and interface morphology with grazing incidence small angle x-ray scattering. Surf Sci Rep. 2009;64:255–380.
[52] Fasolino A, Carra P, Altarelli M. X-ray resonant magnetic scattering from surfaces. Phys Rev B. 1993;47:3877.
[53] Flewett S, Burgos-Parra E, Strelow MG, et al. General treatment of off-specular resonant soft x-ray magnetic scattering using the distorted-wave born approximation: numerical algorithm and experimental studies with hybrid chiral domain structures. Phys Rev B. 2021;103:184401.
[54] Zhang S, Stasinopoulos I, Lancaster T, et al. Room-temperature helimagnetism in FeGe thin films. Sci Rep. 2017;7:1–10.
[55] Huang H, Lee SJ, Kim B, et al. Detection of the chiral spin structure in ferromagnetic $SrRuO_3$ thin film. ACS Appl Mater Interfaces. 2020;12:37757–37763.
[56] Li W, Bykova I, Zhang S, et al. Anatomy of skyrmionic textures in magnetic multilayers. Adv Mater. 2019;31:1807683.
[57] Léveillé C, Flewett S, Burgos-Parra E, et al. Chiral spin spiral in synthetic antiferromagnets probed by circular dichroism in x-ray resonant magnetic scattering. Phys Rev B. 2021;104:L060402.
[58] Kachel T, Eggenstein F, Follath R. A soft x-ray plane-grating monochromator optimized for elliptical dipole radiation from modern sources. J Synchrotron Radiat. 2015;22:1301–1305.
[59] Abrudan RM, Radu F. Alice: a diffractometer/reflectometer for soft x-ray resonant magnetic scattering at bessy ii. J Large Scale Res Facil JLSRF. 2016;2:A69.
[60] Aqeel A, Sahliger J, Li G, et al. Growth and helicity of noncentrosymmetric $Cu_2OSeO_{3\ crystals}$. Phys Status Solidi B. 2022;259:2100152.

[61] Aqeel A, Vera-Marun IJ, van Wees BJ, et al. Surface sensitivity of the spin Seebeck effect. J Appl Phys. 2014;116:153705.
[62] Arnold T, Böhm G, Fechner R, et al. Ultra-precision surface finishing by ion beam and plasma jet techniques—status and outlook. Nucl Instrum Methods Phys Res A. 2010;616:147–156.
[63] Zhang S, Bauer A, Burn D, et al. Multidomain skyrmion lattice state in cu2oseo3. Nano Lett. 2016;16:3285–3291.
[64] Milde P, Köhler L, Neuber E, et al. Field-induced reorientation of helimagnetic order in Cu_2OSeO_3 probed by magnetic force microscopy. Phys Rev B. 2020;102:024426.
[65] Izyumov YA. Modulated, or long-periodic, magnetic structures of crystals. Soviet Phys Uspekhi. 1984;27:845.
[66] Honda T, Yamasaki Y, Nakao H, et al. Topological metastability supported by thermal fluctuation upon formation of chiral soliton lattice in $CrNb_3S_6$. Sci Rep. 2020;10:1–12.
[67] Grigoriev S, Maleyev S, Okorokov A, et al. Field-induced reorientation of the spin helix in MnSi near T_c. Phys Rev B. 2006;73:224440.
[68] Dyadkin V, Prša K, Grigoriev S, et al. Chirality of structure and magnetism in the magnetoelectric compound Cu_2OSeO_3. Phys Rev B. 2014;89:140409.
[69] Eisebitt S, Lörgen M, Eberhardt W, et al. Polarization effects in coherent scattering from magnetic specimen: implications for x-ray holography, lensless imaging, and correlation spectroscopy. Phys Rev B. 2003;68:104419.
[70] Tokunaga Y, Yu XZ, White JS, et al. A new class of chiral materials hosting magnetic skyrmions beyond room temperature. Nat Commun. 2015;6:1–7.
[71] Nayak AK, Kumar V, Ma T, et al. Magnetic antiskyrmions above room temperature in tetragonal heusler materials. Nature. 2017;548:561–566.
[72] Takagi R, Yu XZ, White JS, et al. Low-field bi-skyrmion formation in a noncentrosymmetric chimney ladder ferromagnet. Phys Rev Lett. 2018;120:037203.
[73] Karube K, Peng L, Masell J, et al. Room-temperature antiskyrmions and sawtooth surface textures in a non-centrosymmetric magnet with S4 symmetry. Nat Mater. 2021;20:335–340.